Missing-linker-assisted artesunate delivery by metal-organic frameworks for synergistic cancer treatment

Wang, Dongdong; He, Isabel Wenjia; Liu, Jiawei; Jana, Deblin; Wu, Yinglong; Zhang, Xiaodong; Qian, Cheng; Guo, Yi; Chen, Xiaokai; Bindra, Anivind Kaur; Zhao, Yanli

2021

Wang, D., He, I. W., Liu, J., Jana, D., Wu, Y., Zhang, X., Qian, C., Guo, Y., Chen, X., Bindra, A. K. & Zhao, Y. (2021). Missing-linker-assisted artesunate delivery by metal-organic frameworks for synergistic cancer treatment. Angewandte Chemie International Edition, 60(50), 26254-26259. https://dx.doi.org/10.1002/anie.202112128

https://hdl.handle.net/10356/155942

https://doi.org/10.1002/anie.202112128

RESEARCH ARTICLE

Missing-Linker-Assisted Artesunate Delivery by Metal-Organic Frameworks for Synergistic Cancer Treatment

Dongdong Wang,[a] Isabel Wenjia He,[a] Jiawei Liu,[a] Deblin Jana,[a] Yinglong Wu,[a] Xiaodong Zhang,[a] Cheng Qian,[a] Yi Guo,[a] Xiaokai Chen,[a] Anivind Kaur Bindra,[a] and Yanli Zhao*[a,b]

[a] Dr. D. Wang, I. He, Dr. J. Liu, Dr. D. Jana, Dr. Y. Wu, Dr. X. Zhang, Dr. C. Qian, Dr. Y. Guo, Dr. X. Chen, Dr. A. K. Bindra, Prof. Y. L. Zhao
Division of Chemistry and Biological Chemistry
School of Physical and Mathematical Sciences
Nanyang Technological University
21 Nanyang Link, 637371 Singapore
Email: zhaoyanli@ntu.edu.sg

[b] Prof. Y. L. Zhao
School of Chemical and Biological Engineering
Nanyang Technological University
70 Nanyang Drive, 637459 Singapore

Abstract: *Clinical translation of artesunate (ATS) as a potent antitumor drug has been obstructed by its rapid degradation and low bioavailability. Herein, we report the development of ATS nanomedicine through the self-assembly with $Mn[Co(CN)_6]_{2/3}\square_{1/3}$ metal-organic frameworks (MOFs) having hidden missing linkers. The defects originated from the missing linkers play a key role in increasing the biological stability and tumor accumulation of ATS. Chlorin e6 (Ce6) and ATS can be co-loaded into MOFs for a synergistic antitumor efficacy. In the presence of intracellular HCO_3^-, Mn^{2+} acts as an efficient catalyst to promote the bicarbonate-activated H_2O_2 system and induce oxidative death to cancer cells based on ATS with an endoperoxide bridge. The released $[Co^{III}(CN)_6]$ linker undergoes a redox reaction with intracellular glutathione to prevent the scavenging ability of reactive oxygen species, contributing to synergistic chemodynamic therapy of ATS and photodynamic therapy of Ce6. Thus, defect-engineered MOFs with hidden missing linkers hold great promises in advancing the practical uses of ATS as an antitumor medicine.*

Introduction

Cancer is responsible for one in six deaths globally.[1] Chemotherapy has long served as one of the standard cancer treatment approaches, while it is fraught with significant levels of side effects.[2] Artemisinin and its derivatives, such as artesunate (ATS), as the first-line anti-malarial drugs have recently attracted increasing attentions for being innovative antitumor drugs against various cancer line cells.[3] Unlike chemical-based medicines, natural ones derived from herbs can minimize the side effects to the utmost extent.[4] Nevertheless, the direct utilization of ATS is hindered by rapid degradation under physiological conditions and low bioavailability.[5] Artemisinin and its derivatives with an endoperoxide bridge can react with ferrous-based catalysts to generate free radicals via Fenton-like reaction or molecular rearrangement, inducing oxidative death to cancer cells.[6] Based on this principle, various strategies have been proposed to deliver artemisinin and its derivatives using Fe-based nanoplatforms.[7] The post-synthetic loading strategy usually results in low loading capacity, as drugs are just loaded via physical adsorption on these nanoplatforms. Thus, developing nanosystems that possess high drug loading content, avoid unpredictable drug leakage, and release them only within the lesion sites is of great importance for clinical translation.

Metal-organic frameworks (MOFs) have been recognized as promising platforms for drug delivery on account of their structural diversity, functional tunability, and favorable biocompatibility.[8] The general drug-loading strategy using MOFs is often based on the post-synthetic strategy, resulting in low loading capacity. For many adsorbed pharmaceutical compounds, the defects in MOFs could be the real contributor.[9] Therefore, defect engineering is a feasible approach to construct MOF-based drug delivery systems with controllable loading capacity and responsive releasing profile. For instance, UiO-66 nanoparticles with surface defects showed enhanced loading capacity toward DNA molecules because of the zirconium-phosphate coordination.[10] Recently, Forgan et al. developed a multivariate modulation strategy to accommodate multiple drugs in UiO-66 MOFs through defect loading.[11]

Prussian blue analogues (PBAs) are a diverse family of microporous MOFs with a nominal formula of $M_a[M_b(CN)_6]$.[12] The strong coordination interaction between C≡N and M_b enables good stability and negligible toxicity of the $[M_b(CN)_6]$ linker.[13] For example, Prussian blue has already been approved by U.S. Food and Drug Administration for the treatment of radioactive exposure in clinical practice.[14] As a typical PBA, $Mn^{II}_2[Co^{III}(CN)_6]_3$ can be synthesized via a one-pot self-assembly process. Charge balance requires the total oxidation states of Mn^{II} and Co^{III} sum to 6, similar to $Cd^{II}[Pd^{IV}(CN)_6]$.[15] In $Mn^{II}_2[Co^{III}(CN)_6]_3$, however, the total oxidation state of Mn^{II} and Co^{III} is 5, violating the oxidation-state-sum rule. Consequently, the composition is well approximated by the formula $Mn^{II}[Co^{III}(CN)_6]_{2/3}\square_{1/3}$ (denoted as MC), where the symbol □ represents the hidden $[Co^{III}(CN)_6]$ missing linkers.[16] Geometry dictates that these defects need to form connected neighbor pairs and give an extended pore network, as one-quarter of missing linkers is the threshold to support completely isolated

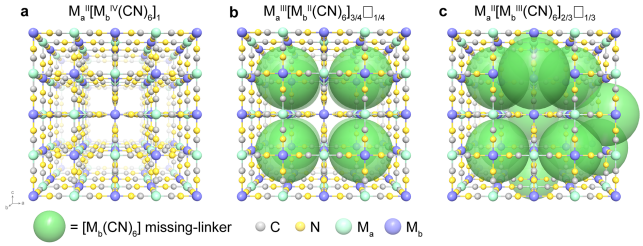

Scheme 1. Schematic illustration of the parent structure (left). In Prussian blue (middle), one-quarter of the $[M_b(CN)_6]$ is vacant, generating isolated micropores (green spheres). In PBAs (right), one-third of the $[M_b(CN)_6]$ is vacant.

vacancy (**Scheme 1**). Those connected defects endow MC with enhanced drug loading capacity through a self-sufficient defect engineering.

Bicarbonate (HCO_3^-)-activated H_2O_2 (BAP) system has shown a great promise in the oxidation of various contaminants under the catalysis of multivalent metal cations in the environmental area.[17] Previous studies indicated that Mn^{2+} showed the highest catalytic reactivity compared to Co^{2+}, Cu^{2+}, and Fe^{2+} for the BAP system.[18] Fortunately, HCO_3^-/CO_2 is one of the most abundant physiological indexes in the living body, thus providing sufficient HCO_3^- to the BAP-like system for Mn^{2+}-activated reactive oxygen species (ROS) generation from ATS.[19] Herein, we show that two drugs (Ce6 and ATS) containing metal-binding carboxylate moiety can be co-loaded into MC (named as MCCA), taking advantage of the one-third of missing linkers. Upon the internalization by cancer cells, the cargos were released under a high glutathione (GSH) condition. Mn^{2+} acts as an efficient catalyst to activate the BAP-like system and induce oxidative death to cancer cells from ATS with an endoperoxide bridge in the presence of intracellular HCO_3^- (**Scheme 2**). The released $[Co^{III}(CN)_6]$ linkers undergo a redox reaction with intracellular GSH to prevent its ROS scavenging ability. In addition, the high-spin Mn_6-vacancy (S = 5/2) moiety endows MCCA a T_1-magnetic resonance (T_1-MR) imaging agent. Altogether, the hidden missing-linker-assisted loading strategy simultaneously increases tumor accumulation of both drugs, contributing to a synergistic antitumor efficacy.

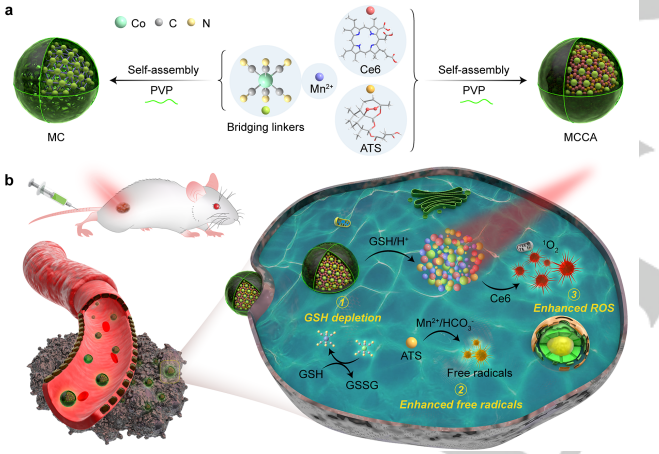

Scheme 2. a) Schematic illustration of the one-pot self-assembly synthesis of MCCA nanomedicine by taking advantage of the hidden missing linkers. b) Mechanism of MCCA for synergistic therapy.

Results and Discussion

The MC MOFs with intrinsic missing linkers were fabricated via a one-pot self-assembly strategy on account of the coordination interaction between N-terminated $[Co^{III}(CN)_6]$ linker and Mn ion. In MC MOFs, one-third of $[Co^{III}(CN)_6]$ is vacant. Those vacancies should connect by each other to give an extended porous network.[16] Consequently, MC might be an excellent system for cargo loading. Herein, we chose two model drugs, Ce6 and ATS, both of which contain metal-binding carboxylate moiety. Through the control of initial feeding process, Ce6 loaded MC MOFs (MCC), ATS loaded MC MOFs (MCA), as well as Ce6 and ATS co-loaded MOFs (MCCA) were also synthesized. For comparison,

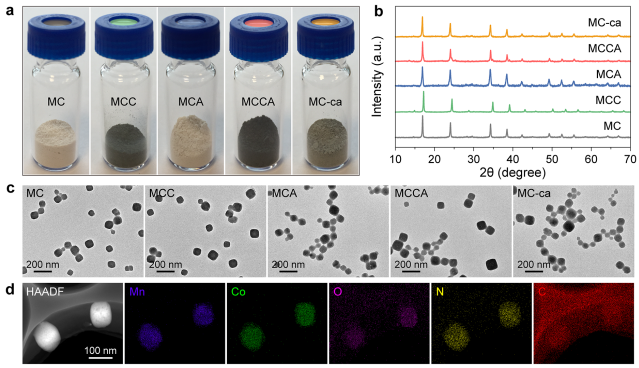

Figure 1. a) Photograph of MC, MCC, MCA, MCCA, and MC-ca. b) Powder XRD patterns of different formulations. c) TEM images of these formulations. d) HAADF-STEM image and corresponding energy dispersive X-ray spectroscopy elemental mapping of MCCA nanomedicine.

a post-synthetic loading strategy was used to load Ce6 and ATS (MC-ca) (**Figure 1a**). No significant change in the powder X-ray diffraction (XRD) patterns was detected among different samples, indicating no influences of Ce6 and ATS loading on the MOF crystallinity (Figure 1b). The successful loading of Ce6 and ATS was further verified by Fourier-transform infrared spectroscopy, thermogravimetric analysis, and Brunauer-Emmett-Teller surface area analysis (Figure S1-S3).

UV-vis-NIR spectra showed a shift of Ce6 absorbance peak in the self-assembled system, indicating the interaction between Mn and protonated carboxylate groups as well as the π-π stacking interaction between drugs and bridging linkers (Figure S4). The loading capacity of Ce6 in MCC, MCCA, and MC-ca was calculated to be 28.6, 22.4, and 3.5 wt%, respectively (Figure S5 and Table S1). The loading capacity of ATS in MCA, MCCA, and MC-ca was calculated to be 24.5, 18.2, and 1.3 wt%, respectively (Figure S6). Scanning electron microscopy (SEM) and transmission electron microscopy (TEM) were performed to study the morphology (Figure 1c and S7). High-angle annular dark field scanning transmission electron microscopy (HAADF-STEM) images revealed a uniform distribution of Mn, Co, O, N, and C elements through the MCCA nanoparticles (Figure 1d). The zeta potentials of MC and MCCA were measured to be -13.5 and -10.7 mV (Figure S8). The average hydrodynamic diameters of MC and MCCA were determined to be 100.4 ± 2.9 nm and 113.2 ± 7.6 nm (Figure S9). No aggregation was observed over time after the storage in different physiological buffers (Figure S10).

It is well known that tumor cells maintain a high GSH level (4-10 folds) compared to normal cells.[20] Moreover, clinical trials have shown that high GSH level plays a significant role in drug resistance during ROS-based tumor therapy.[21] The as-prepared MCCA exhibited a time-dependent degradation at pH 5.0 and GSH concentration of 8 mM within 48 h incubation (**Figure 2a**). Simultaneously, MCCA displayed 84.4% Ce6 release in the presence of GSH (8 mM) at a pH 5.0, while only 5.1% Ce6 was liberated at pH 7.4 without GSH (Figure 2b). These results demonstrated that high GSH condition is mainly responsible to the release on account of the competitive coordination of intracellular GSH with Mn^{2+}.[22] It is noteworthy that low pH contributes to only partial drug release due to the protonation of COO^- group of Ce6 molecule that could coordinate to the MOF frameworks. Moreover, the released $[Co^{III}(CN)_6]$ linkers with central Co^{III} would deplete GSH. The GSH-depletion ability was

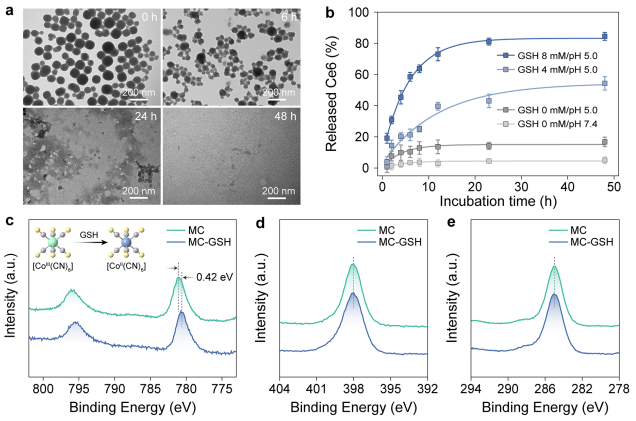

Figure 2. a) TEM images of MCCA after incubation for different periods of time in PBS (pH = 5.0, [GSH] = 8 mM). b) Time-dependent Ce6 release profile from MCCA upon the exposure to different stimuli. c) XPS Co 2p spectra of MC and MC after GSH treatment. d,e) XPS N 1s and C 1s spectra of MC and MC after GSH treatment.

studied by X-ray photoelectron spectroscopy (XPS). After GSH treatment, the Co 2p XPS peak of MC showed a 0.3 eV shift to lower energy level, suggesting the reduction from Co^{III} to Co^{II} (Figure 2c and S11). In contrast, C 1s and N 1s showed no obvious changes (Figure 2d,e). Moreover, ^1H NMR spectra showed the generation of glutathione disulfide (GSSG) from GSH in the presence of $[Co(CN)_6]$ linkers (Figure S12).

In vitro cytotoxicities of $[Co(CN)_6]$ linker and MC were assessed by MTT assay. The viability of 4T1 cells still maintained over 88% even at a high concentration of 100 ppm (Figure S13). CLSM images demonstrated a time-dependent internalization of MCCA (**Figure 3a**). The Pearson's colocalization coefficients between Ce6 and Lyso-tracker for 1 h, 4 h, and 8 h were calculated to be 0.48 ± 0.02, 0.61 ± 0.02, and 0.52 ± 0.13, respectively. The increased colocalization coefficients from 1 h to 4 h implied MCCA escaped from early endosome and accumulated in lysosome. The decreased colocalization coefficient at 8 h indicated the diffusion from lysosome into cytoplasm.[23] In addition, the quantification of cellular uptake using flow cytometry was consistent with the CLSM results (Figure S14). Furthermore, the intracellular GSH-depletion of MCCA was studied using a thiol-tracker. In the presence of MCCA, a 3.85-fold reduction in the GSH level was observed compared to control group (Figure 3b,c). The cytotoxicity of ATS against 4T1 cells under the catalysis of different metal ions (Co^{2+}, Fe^{2+}, Cu^{2+}, and Mn^{2+}) was explored, showing enhanced cytotoxicity of ATS in the presence of Mn^{2+} (Figure 3d). This phenomenon is consistent with the previous report that Mn^{2+} catalyst exhibits enhanced oxidation ability in the BAP system.[24] Free ATS showed limited antitumor efficacy due to the low availability of exogenous metal ions (Figure 3e). In contrast, MCA presented a concentration-dependent killing effect. Under an ATS concentration of 16 ppm, the killing efficacy was 56.8%, much higher than that of free ATS with a value of 15%. These results highlighted the GSH-depletion and ROS generation abilities of the Mn^{2+}-activated BAP-like system. Furthermore, by combining with photodynamic therapy, the killing efficiency of MCCA reached as high as 87.1% (Figure 3f). The intracellular oxidative stress was studied with 2',7'-dichlorodihydrofluorescein diacetate (H_2-DCFDA) as an indicator. MCCA-treated cells exhibited the highest ROS level with 13.85-folds higher than the control group (Figure 3g,h). Moreover, live/dead staining results showed similar tendency (Figure 3i). These results demonstrated the enhanced antitumor ability of Mn^{2+}-activated chemodynamic therapy and photodynamic therapy.

The results of hemolysis test indicated no noticeable hemolytic effect even with a high MCCA concentration of 1000 ppm, indicating its excellent biocompatibility in blood (Figure S15). Thereafter, the tumor accumulation ability of MCCA was studied by in vivo fluorescence imaging. After systematic administration of free Ce6 and MCCA, fluorescence signals were monitored during the following 24 h. Compared with Ce6, MCCA showed enhanced fluorescence signals within the tumor site on account of the well-known enhanced permeability and retention effect (**Figure 4a**).[25] Furthermore, ex vivo biodistribution study at 24 h post-injection indicated a maximum accumulation in tumor tissue, followed by liver, kidney, spleen (Figure 4b,c). Notably, the liver, kidney, and spleen revealed relatively higher fluorescence, indicating the active uptake by the reticuloendothelial system.[26] Due to the existence of missing linkers, the unsaturated Mn with the high-spin state (S = 5/2) endows MCCA a potential T_1-MR imaging agent.[27] MCCA nanoparticles were intravenously injected into 4T1 tumor-bearing mice, followed by in vivo MR imaging. The tumor site exhibited brighter T_1-MR signals at 24 h post-injection (Figure 4d). Therefore, both fluorescence and MR imaging indicated the efficient tumor accumulation of MCCA.

Additionally, no detectable pathological abnormality was found in major organs from hematoxylin and eosin (H&E) staining, indicating its minimal adverse effects (Figure 4e). To further ensure the biosafety, healthy Balb/c mice were intravenously administrated with MCCA before performing serum chemistry and hematological index analyses. All indexes showed no distinct

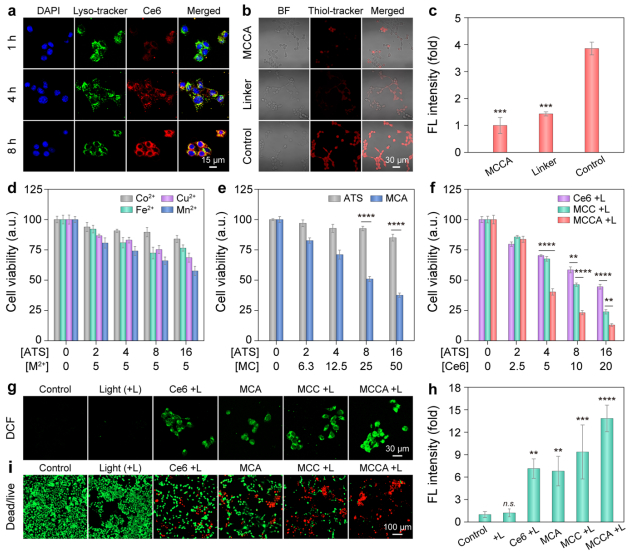

Figure 3. a) Confocal laser scanning microscopy (CLSM) images of 4T1 cells showing time-dependent uptake of MCCA. b) CLSM images of intracellular GSH with thiol-tracker as an indicator after different treatments. c) Quantitative fluorescence intensity of thiol-tracker. d) MTT cell viability of metal ion-activated chemodynamic therapy of ATS. e) MTT cell viability of pure ATS and MCA. f) In vitro antitumor of free Ce6, MCC, and MCCA under irradiation with 660-nm LED light (+L, 10 mW cm^{-2}, 5 min). g) Intracellular ROS generation after different treatments. h) Quantitative fluorescence intensity of DCF. i) Live/dead staining of 4T1 cells. Green represents live cells and red represents dead cells. FL: fluorescence. Statistical analysis was performed by one-way ANOVA (*p < 0.05, **p < 0.01, ***p < 0.001, ****p < 0.001, *n.s.*: not significant).

abnormalities between MCCA and control groups, indicating no significant inflammation, infection, and side effects of MCCA on the hematological system (Figure S16).[28]

Therapy studies were also performed on 4T1 tumor-bearing Balb/c mice. Mice were randomly divided into five groups: PBS (group I), free ATS plus free Ce6 (group II), MCA (group III), MCC (group IV), and MCCA (group V). Groups II, IV, and V were treated with 660 nm light irradiation. Compared to the control group, intravenous administration of both free ATS and Ce6 showed limited inhibition due to their low bioavailability (**Figure 5a**). The MCA and MCC groups exhibited higher anticancer ability because of corresponding chemodynamic and photodynamic effect (Figure 5b). In contrast, MCCA presented the best antitumor efficacy on account of the combined effect. The combination effect using Bliss independence model indicated that the observed inhibition rate (87.72%) was higher than the predicted inhibition rate (83.76%), demonstrating a synergistic effect (see the Supporting Information for details). At the end of the treatment, all tumors were collected and weighed (Figure 5c). The results were consistent with the tumor growth curves. Furthermore, no detectable variation in average body weight was observed for all five groups during the treatment process (Figure 5d), suggesting the favorable biocompatibility of all formulations. The generated ROS within tumor sites from different groups was also studied, indicating much higher green fluorescence signals in MCCA-treated tumor tissue than MCA or MCC-treated ones (Figure 5e). The terminal deoxynucleotidyl transferase dUTP nick end labeling (TUNEL) staining results revealed elevated levels of apoptotic cells in MCA, MCC, and MCCA-treated tumors, while having little apoptotic cells in the control group (Figure 5f). Semi-quantitative analysis of the TUNEL positive area for the MCCA group was 50.44%, much higher than MCC (29.97%) and MCA (25.91%) groups (Figure S17). All these results demonstrated the superior in vivo antitumor capacity of MCCA nanomedicine.

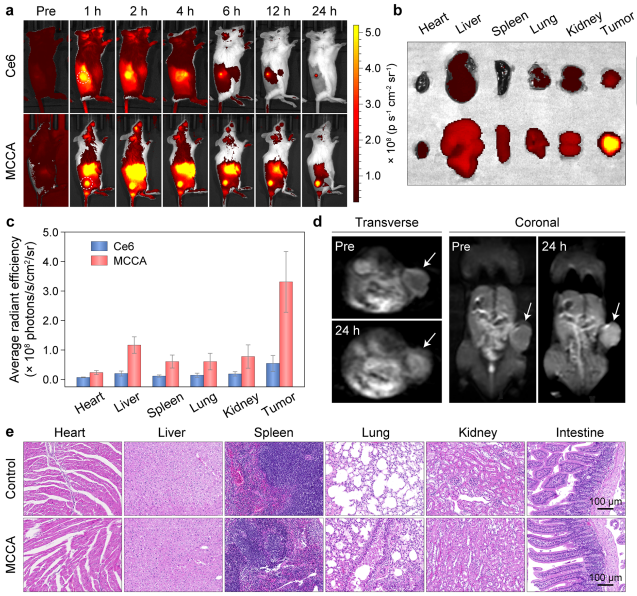

Figure 4. a) Fluorescence imaging of 4T1 tumor-bearing mice (white dotted circles) after intravenous injection of Ce6 and MCCA. b) Ex vivo fluorescence imaging of main organs and tumor tissues at 24 h post-injection. c) Average radiant efficiency of main organs and tumors. d) In vivo T_1-MR imaging of mice before and at 24 h post-injection in transverse and coronal sections. e) H&E staining images from main organs of mice treated with PBS and MCCA.

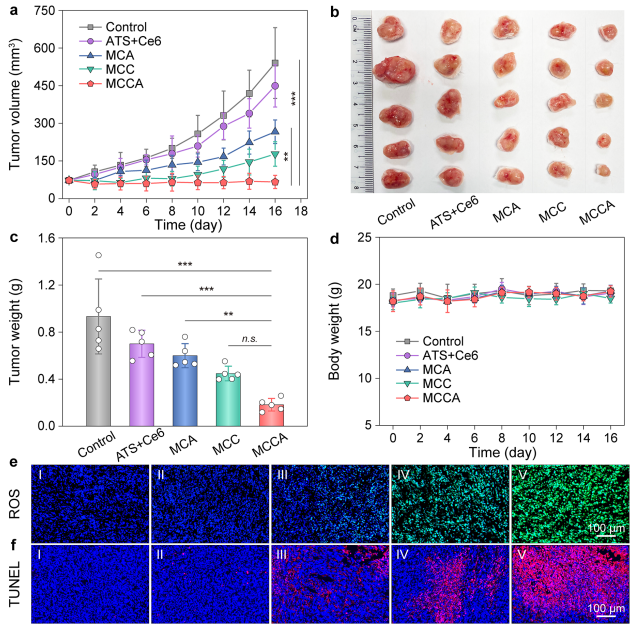

Figure 5. a) Average tumor volume (n = 5) of each group during the treatment. b) Photograph of tumors harvested at the end of treatment. c) Weight of harvested tumors from different groups at the end of treatment. d) Average body weight of mice from different groups. e,f) ROS staining (green fluorescence) and TUNEL staining (red fluorescence) of tumor tissues from different treatment groups. The nuclei were stained by 4',6-diamidino-2-phenylindole (blue fluorescence). Statistical analysis was performed by one-way ANOVA (**p < 0.01, ***p < 0.001, *n.s.*: not significant).

Conclusion

In summary, we have developed a dual-drug-loading nanoagent via a facile one-pot self-assembly strategy by taking advantage of the hidden missing linkers within MC MOFs. The hidden missing-linker-assisted loading strategy simultaneously increases the stability and tumor accumulation of ATS and Ce6 with a loading capacity of 18.2 and 22.4 wt%, respectively. In the presence of abundant physiological CO_2/HCO_3^-, Mn^{2+} acts as an excellent catalyst to activate the BAP-like system and induce oxidative death to cancer cells resulted from ATS with an endoperoxide bridge. Moreover, the released organic linkers undergo a redox reaction with intracellular GSH to prevent ROS scavenging, leading to enhanced synergistic chemodynamic and photodynamic therapy of cancer. Our results show that defect-engineering MOFs with hidden missing linkers hold a great promise in advancing the future clinical applications of ATS as an antitumor medicine.

Acknowledgements

This research is supported by the Singapore Agency for Science, Technology and Research (A*STAR) AME IRG grant (A20E5c0081) and the Singapore National Research Foundation Investigatorship (NRF-NRFI2018-03).

Conflict of interest

The authors declare no conflict of interests.

Keywords: artesunate • metal-organic frameworks • missing linkers • self-assembly • synergistic cancer therapy

[1] WHO Report on Cancer, *World Health Organization* **2020**.

[2] a) L. Kelland, *Nat. Rev. Cancer* **2007**, *7*, 573-584; b) N. P. Staff, A. Grisold, W. Grisold, A. J. Windebank, *Ann. Neurol.* **2017**, *81*, 772-781.

[3] a) Y. Tu, *Nat. Med.* **2011**, *17*, 1217-1220; b) D. Chaturvedi, A. Goswami, P. P. Saikia, N. C. Barua, P. G. Rao, *Chem. Soc. Rev.* **2010**, *39*, 435-454; c) D. L. Klayman, *Science* **1985**, *228*, 1049-1055; d) N. Cordes, T. Efferth, M. Giaisi, A. Merling, P. H. Krammer, M. Li-Weber, *PLoS One* **2007**, *2*, e693; e) X. Duan, C. Chan, W. Han, N. Guo, R. R. Weichselbaum, W. Lin, *Nat. Commun.* **2019**, *10*, 1899.

[4] a) H. Zhang, L. Hou, X. Jiao, Y. Ji, X. Zhu, Z. Zhang, *Biomaterials* **2015**, *37*, 353-366; b) B. H. Kiani, W. K. Kayani, A. U. Khayam, E. Dilshad, H. Ismail, B. Mirza, *Mol. Biol. Rep.* **2020**, *47*, 6321-6336.

[5] Y. Chen, X. Lin, H. Park, R. Greever, *Nanomed. Nanotechnol. Biol. Med.* **2009**, *5*, 316-322.

[6] a) A. Robert, J. Cazelles, B. Meunier, *Angew. Chem. Int. Ed.* **2001**, *40*, 1954-1957; b) M. Asano, H. Iwahashi, *Eur. J. Med. Chem.* **2017**, *127*, 740-747; c) G. Bai, Y. Gao, S. Liu, S. Shui, G. Liu, *Free Radical Biol. Med.* **2021**, *163*, 234-242.

[7] a) J. Chen, Z. Guo, H. B. Wang, J. J. Zhou, W. J. Zhang, Q. W. Chen, *Biomaterials* **2014**, *35*, 6498-6507; b) D. Wang, J. Zhou, R. Chen, R. Shi, G. Zhao, G. Xia, R. Li, Z. Liu, J. Tian, H. Wang, Z. Guo, H. Wang, Q. Chen, *Biomaterials* **2016**, *100*, 27-40; c) J. Bai, X. Jia, W. Zhen, W. Cheng, X. Jiang, *J. Am. Chem. Soc.* **2018**, *140*, 106-109; d) X. Wan, H. Zhong, W. Pan, Y. Li, Y. Chen, N. Li, B. Tang, *Angew. Chem. Int. Ed.* **2019**, *58*, 14134-14139.

[8] a) P. Horcajada, R. Gref, T. Baati, P. K. Allan, G. Maurin, P. Couvreur, G. Ferey, R. E. Morris, C. Serre, *Chem. Rev.* **2012**, *112*, 1232-1268; b) D. Wang, D. Jana, Y. Zhao, *Acc. Chem. Res.* **2020**, *53*, 1389-1400; c) M. X. Wu, Y. W. Yang, *Adv. Mater.* **2017**, *29*, 1606134; d) K. Ni, G. Lan, C. Chan, B. Quigley, K. Lu, T. Aung, N. Guo, P. La Riviere, R. R. Weichselbaum, W. Lin, *Nat. Commun.* **2018**, *9*, 2351. e) X. G. Wang, L. Xu, M. J. Li, X. Z. Zhang, *Angew. Chem. Int. Ed.* **2020**, *59*, 18078-18086.

[9] a) M. He, J. Zhou, J. Chen, F. Zheng, D. Wang, R. Shi, Z. Guo, H. Wang, Q. Chen, *J. Mater. Chem. B* **2015**, *3*, 9033-9042; b) D. Wang, J. Zhou, R. Shi, H. Wu, R. Chen, B. Duan, G. Xia, P. Xu, H. Wang, S. Zhou, C. Wang, H. Wang, Z. Guo, Q. Chen, *Theranostics* **2017**, *7*, 4605-4617.

[10] a) S. Wang, C. M. McGuirk, M. B. Ross, S. Wang, P. Chen, H. Xing, Y. Liu, C. A. Mirkin, *J. Am. Chem. Soc.* **2017**, *139*, 9827-9830; b) Z. Wang, Y. Fu, Z. Kang, X. Liu, N. Chen, Q. Wang, Y. Tu, L. Wang, S. Song, D. Ling, H. Song, X. Kong, C. Fan, *J. Am. Chem. Soc.* **2017**, *139*, 15784-15791.

[11] I. Abanades Lazaro, C. J. R. Wells, R. S. Forgan, *Angew. Chem. Int. Ed.* **2020**, *59*, 5211-5217.

[12] a) H. J. Buser, D. Schwarzenbach, W. Petter, A. Ludi, *Inorg. Chem.* **2002**, *16*, 2704-2710; b) S. S. Kaye, J. R. Long, *J. Am. Chem. Soc.* **2005**, *127*, 6506-6507; c) D. Wang, H. Wu, S. Z. F. Phua, G. Yang, W. Q. Lim, L. Gu, C. Qian, H. Wang, Z. Guo, H. Chen, Y. Zhao, *Nat. Commun.* **2020**, *11*, 357.

[13] a) M. Hu, S. Furukawa, R. Ohtani, H. Sukegawa, Y. Nemoto, J. Reboul, S. Kitagawa, Y. Yamauchi, *Angew. Chem. Int. Ed.* **2012**, *51*, 984-988; b) M. Shokouhimehr, E. S. Soehnlen, A. Khitrin, S. Basu, S. D. Huang, *Inorg. Chem. Commun.* **2010**, *13*, 58-61.

[14] a) W. Wu, L. Yu, Y. Pu, H. Yao, Y. Chen, J. Shi, *Adv. Mater.* **2020**, *32*, 2000542; b) G. Fu, W. Liu, S. Feng, X. Yue, *Chem. Commun.* **2012**, *48*, 11567-11569.

[15] H. J. Buser, G. Ron, A. Ludi, P. Engel, *J. Chem. Soc., Dalton Trans.* **1974**, 2473-2474.

[16] A. Simonov, T. De Baerdemaeker, H. L. B. Bostrom, M. L. Rios Gomez, H. J. Gray, D. Chernyshov, A. Bosak, H. B. Burgi, A. L. Goodwin, *Nature* **2020**, *578*, 256-260.

[17] a) B. S. Lane, M. Vogt, V. J. DeRose, K. Burgess, *J. Am. Chem. Soc.* **2002**, *124*, 11946-11954; b) A. Jawad, Z. Chen, G. Yin, *Chinese J. Catal.* **2016**, *37*, 810-825.

[18] a) Z. H. Meng, S. H. Wu, S. W. Sun, Z. Xu, X. C. Zhang, X. M. Wang, Y. Liu, H. T. Ren, S. Y. Jia, H. Bai, X. Han, *Inorg. Chem.* **2020**, *59*, 3171-3180; b) E. Illes, A. Mizrahi, V. Marks, D. Meyerstein, *Free Radical Bio. Med.* **2019**, *131*, 1-6.

[19] a) P. T. Bonar, J. R. Casey, *Channels* **2008**, *2*, 337-345; b) L. S. Lin, J. Song, L. Song, K. Ke, Y. Liu, Z. Zhou, Z. Shen, J. Li, Z. Yang, W. Tang, G. Niu, H. H. Yang, X. Chen, *Angew. Chem. Int. Ed.* **2018**, *57*, 4902-4906.

[20] a) P. Kuppusamy, H. Li, G. Ilangovan, A. J. Cardounel, J. L. Zweier, K. Yamada, M. C. Krishna, J. B. Mitchell, *Cancer Res.* **2002**, *62*, 307-312; b) L. Su, R. Li, S. Khan, R. Clanton, F. Zhang, Y. N. Lin, Y. Song, H. Wang, J. Fan, S. Hernandez, A. S. Butters, G. Akabani, R. MacLoughlin, J. Smolen, K. L. Wooley, *J. Am. Chem. Soc.* **2018**, *140*, 1438-1446.

[21] a) M. Diehn, R. W. Cho, N. A. Lobo, T. Kalisky, M. J. Dorie, A. N. Kulp, D. Qian, J. S. Lam, L. E. Ailles, M. Wong, B. Joshua, M. J. Kaplan, I. Wapnir, F. M. Dirbas, G. Somlo, C. Garberoglio, B. Paz, J. Shen, S. K. Lau, S. R. Quake, J. M. Brown, I. L. Weissman, M. F. Clarke, *Nature* **2009**, *458*, 780-783; b) J. M. Estrela, A. Ortega, E. Obrador, *Crit. Rev. Clin. Lab. Sci.* **2006**, *43*, 143-181; c) E. A. Bump, N. Y. Yu, J. M. Brown, *Science* **1982**, *217*, 544-545.

[22] H. Zhang, K. Liu, S. Li, X. Xin, S. Yuan, G. Ma, X. Yan, *ACS Nano* **2018**, *12*, 8266-8276.

[23] Z. Liu, L. Zhang, T. Cui, M. Ma, J. Ren, X. Qu, *Angew. Chem. Int. Ed.* **2021**, *60*, 15436-15444.

[24] E. Ember, S. Rothbart, R. Puchta, R. van Eldik, *New J. Chem.* **2009**, *33*, 34-49.

[25] a) J. Fang, H. Nakamura, H. Maeda, *Adv. Drug Delivery Rev.* **2011**, *63*, 136-151; b) S. K. Hobbs, W. L. Monsky, F. Yuan, W. G. Roberts, L. Griffith, V. P. Torchilin, R. K. Jain, *Proc. Natl. Acad. Sci. U. S. A.* **1998**, *95*, 4607-4612.

[26] a) W. Poon, Y. N. Zhang, B. Ouyang, B. R. Kingston, J. L. Y. Wu, S. Wilhelm, W. C. W. Chan, *ACS Nano* **2019**, *13*, 5785-5798. b) G. Yang, S. Z. F. Phua, A. K. Bindra, Y. Zhao, *Adv. Mater.* **2019**, *31*, 1805730. c) X. Zhang, X. Chen, Y. Guo, G. Gao, D. Wang, Y. Wu, J. Liu, G. Liang, Y. Zhao, F. Wu, *Angew. Chem. Int. Ed.* **2021**, *60*, 14013-14021.

[27] a) M. Cammarata, S. Zerdane, L. Balducci, G. Azzolina, S. Mazerat, C. Exertier, M. Trabuco, M. Levantino, R. Alonso-Mori, J. M. Glownia, S. Song, L. Catala, T. Mallah, S. F. Matar, E. Collet, *Nat. Chem.* **2021**, *13*, 10-14; b) D. Wang, H. Wu, C. Wang, L. Gu, H. Chen, D. Jana, L. Feng, J. Liu, X. Wang, P. Xu, Z. Guo, Q. Chen, Y. Zhao, *Angew. Chem. Int. Ed.* **2021**, *60*, 3001-3007.

[28] a) P. Xu, H. Wu, D. Wang, G. Zhao, F. Li, B. Qiu, Z. Guo, Q. Chen, *Adv. Healthcare Mater.* **2018**, *7*, 1800322; b) J. Liu, Y. Yang, W. Zhu, X. Yi, Z. Dong, X. Xu, M. Chen, K. Yang, G. Lu, L. Jiang, Z. Liu, *Biomaterials* **2016**, *97*, 1-9.

Table of Contents

COMMUNICATION

Self-assembled nanomedicine based on metal-organic frameworks (MOFs) with hidden missing linkers shows enhanced artesunate and photosensitizer co-loading capacity. In the presence of abundant physiological HCO_3^-, Mn^{2+} from MOFs catalyzes artesunate with an endoperoxide bridge, inducing oxidative death to cancer cells. Released linkers undergo a redox reaction with intracellular glutathione, contributing to synergistic tumor therapy.

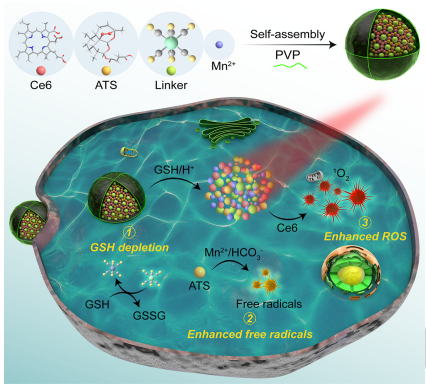

*D. Wang, I. He, J. Liu, D. Jana, Y. Wu, X. Zhang, C. Qian, Y. Guo, X. Chen, A. K. Bindra, and Y. L. Zhao**

Page No. – Page No.

Missing-Linker-Assisted Artesunate Delivery by Metal-Organic Frameworks for Synergistic Cancer Treatment